Title

Transport and Loss of Ring Current Electrons Inside Geosynchronous Orbit During the 17 March 2013 Storm.

Journal

Journal of geophysical research. Space physics, 124(2)

ISSN

2169-9380

Authors

Aseev, NA
Shprits, YY
Wang, D
et al.

Publication Date

2019-02-01

DOI

10.1029/2018ja026031

Peer reviewed

JGR Space Physics

RESEARCH ARTICLE
10.1029/2018JA026031

Transport and Loss of Ring Current Electrons Inside Geosynchronous Orbit During the 17 March 2013 Storm

N. A. Aseev[1,2], Y. Y. Shprits[1,2,3], D. Wang[1], J. Wygant[4], A. Y. Drozdov[3], A. C. Kellerman[3], and G. D. Reeves[5]

[1]GFZ German Research Centre for Geosciences, Potsdam, Germany, [2]Institute of Physics and Astronomy, University of Potsdam, Potsdam, Germany, [3]Department of Earth, Planetary, and Space Sciences, University of California, Los Angeles, CA, USA, [4]School of Physics and Astronomy, University of Minnesota, Minneapolis, MN, USA, [5]Los Alamos National Laboratory, Los Alamos, NM, USA

Abstract Ring current electrons (1–100 keV) have received significant attention in recent decades, but many questions regarding their major transport and loss mechanisms remain open. In this study, we use the four-dimensional Versatile Electron Radiation Belt code to model the enhancement of phase space density that occurred during the 17 March 2013 storm. Our model includes global convection, radial diffusion, and scattering into the Earth's atmosphere driven by whistler-mode hiss and chorus waves. We study the sensitivity of the model to the boundary conditions, global electric field, the electric field associated with subauroral polarization streams, electron loss rates, and radial diffusion coefficients. The results of the code are almost insensitive to the model parameters above 4.5 $R_E R_E$, which indicates that the general dynamics of the electrons between 4.5 R_E and the geostationary orbit can be explained by global convection. We found that the major discrepancies between the model and data can stem from the inaccurate electric field model and uncertainties in lifetimes. We show that additional mechanisms that are responsible for radial transport are required to explain the dynamics of ≥40-keV electrons, and the inclusion of the radial diffusion rates that are typically assumed in radiation belt studies leads to a better agreement with the data. The overall effect of subauroral polarization streams on the electron phase space density profiles seems to be smaller than the uncertainties in other input parameters. This study is an initial step toward understanding the dynamics of these particles inside the geostationary orbit.

Plain Language Summary The dynamics of the ring current electrons is a competition between loss and transport processes in the Earth's inner magnetosphere. These processes remain poorly understood due to difficulties of in situ particle measurements. Given the scarcity of satellite data, numerical modeling is a powerful approach that allows us to gain a deeper insight into the behavior of the ring current electrons. In this work, we investigate which processes dominate the dynamics of these particles within the geostationary orbit. We use the four-dimensional Versatile Electron Radiation Belt code to model electron loss and transport processes during 17 March 2013 geomagnetic storm. To understand the significance of the model uncertainty, we run an ensemble of simulations with different model parameters and compare results with the Van Allen Probe satellite observations. We show that the global convective electric and magnetic fields control the transport of the ring current electrons inside the geostationary orbit. This work is a basis for future studies, which will be extended further away from the Earth and include more comprehensive plasma wave models.

Key Points:
- Ring current electron dynamics within geostationary orbit is modeled and the sensitivity of the model to the input parameters is explored
- Global convective electron transport from geostationary orbit to 4.5 R_E can explain Van Allen Probe observations
- Model results below 4.5 R_E are most sensitive to the electric field and electron lifetimes

Supporting Information:
- Text S1

Correspondence to:
N. A. Aseev,
nikita.aseev@gfz-potsdam.de

Citation:
Aseev, N. A., Shprits, Y. Y., Wang, D., Wygant, J., Drozdov, A. Y., Kellerman, A. C., & Reeves, G. D. (2019). Transport and loss of ring current electrons inside geosynchronous orbit during the 17 March 2013 storm. *Journal of Geophysical Research: Space Physics*, *124*, 915–933. https://doi.org/10.1029/2018JA026031

Received 24 AUG 2018
Accepted 14 JAN 2019
Accepted article online 21 JAN 2019
Published online 1 FEB 2019

1. Introduction

The ring current electrons (energies from ~1 to a few 100 keV) can contribute to surface charging of satellites and may provide from 10% to 25% of the ring current energy during storm times (Frank, 1967; Liu et al., 2005; Zhao et al., 2016). The injections of ~ 10-keV electrons in the inner magnetosphere during enhanced magnetospheric convection excite chorus waves (Hwang et al., 2007; Thorne, 2010), which resonate with relativistic electrons in the radiation belts and provide an effective mechanism of their pitch angle scattering (Albert, 2005; Horne & Thorne, 2003; Shprits et al., 2008; Thorne, 2010) and local acceleration (Horne & Thorne, 1998; Horne et al., 2005; Li et al., 2007; Reeves et al., 2013; Summers et al., 1998). Electrons of

1- to 10-keV energies can be deposited into protective shielding of satellites operating within the ring current region, cause surface charging, and ultimately damage satellite electronics (Baker, 2000; Choi et al., 2011; DeForest, 1972; Ganushkina et al., 2017; Thomsen et al., 2013).

Despite the important role of the ring current electrons, their transport and loss processes within the geosynchronous orbit (GEO) remain poorly understood primarily due to the limited number of measurements. Only several years ago, the Van Allen Probes opened up a whole new opportunity for quantitative tests of models and theory. Reeves et al. (2016) analyzed the Van Allen Probe electron flux measurements and showed the coherence of the particle dynamics across a broad range of energies from a few tens of kiloelectron volts up to megaelectron volts. They found that at any given L shell, the number of enhancement events increases with the decrease in electron energy and the enhancements have an upper energy limit that varies from event to event. Zhao et al. (2016) examined the dynamics of the ring current electrons during storm times in comparison with the ions. Their results indicate that the electrons frequently penetrate deep into the inner magnetosphere and stay in the low-L region for a long time, while the loss of tens of kiloelectron-volt protons is much faster at low L shells. They also found that the contribution of the ring current electrons to the *Dst* index is noticeably smaller than that of the ions. Using the Van Allen Probe observations between December 2012 and September 2013, Turner et al. (2015) found 47 events with signatures of electron injections at L shells ≤ 4, which were limited in energy to $\leq$250 keV and followed the observations of the injections at higher L shells. They also noted that it is often difficult to distinguish electron injections from the enhanced convection during storms.

It still remains unclear which mechanisms are responsible for the earthward transport of ring current electrons within GEO. It was suggested that the global dawn-dusk electric field, driven by the dayside reconnection and antisunward magnetic field line convection, together with corotation-driven radial electric field, defines the electron drift path in the inner magnetosphere (e.g., Axford, 1969; Lyons & Williams, 1984, and references therein). Supporting this theory, Korth et al. (1999) found that lines demarcating enhanced electron flux at GEO match the Alfvén boundaries (the boundaries between open and closed drift trajectories) calculated using the Volland-Stern global electric field model (Stern, 1975; Volland, 1973). Using polar data, Friedel et al. (2001) showed that electrons are organized by the Alfvén boundaries within GEO, shrinking and allowing deeper access of plasma during storm times.

It was proposed that energetic electrons can be injected in the magnetotail during geomagnetically active times by substorm-related localized bursty bulk flows (BBFs; Angelopoulos et al., 1992, 1994; Runov et al., 2009, 2011). Gabrielse et al. (2012) showed that the injections are driven by narrow channels of enhanced electric field associated with the BBFs. However, the efficiency of this transport mechanism to inject particles inside GEO still remains uncertain. Dubyagin et al. (2011) found that a significant fraction of flow bursts is unable to penetrate within 9 R_E, and Ohtani et al. (2006) concluded that only a small portion of BBFs can reach geostationary distances. Further studies (Liu et al., 2016; Sergeev et al., 2012) established that many BBFs are not accompanied by particle injections. Liu et al. (2016) showed that only 20 of 71 events of dipolarization fronts detected within GEO between 1 November 2012 and 1 November 2013 were associated with energetic electron injections, typically not propagating closer than ~6 R_E.

An increase in the large-scale electric field between $L = 3$ and $L = 6$, where L is McIlwain L shell, for moderate to active geomagnetic conditions ($Kp > 3$) was reported by Rowland and Wygant (1998). They showed that during the strongest geomagnetic activity the enhanced electric field can be observed inside $L = 3$. Later, their results were confirmed by Califf et al. (2014). The enhancement was attributed to subauroral polarization streams (SAPS; e.g., Foster & Burke, 2002; Foster & Vo, 2002), the northward middle-latitude ionospheric electric field that arise from the separation between earthward ion and electron plasma sheet boundaries (Southwood & Wolf, 1978) and usually pronounced in the evening sector. Although initial steps were made in order to understand how SAPS affect electrons in the inner magnetosphere (Califf et al., 2017; Lejosne et al., 2018; Su et al., 2016), more comprehensive modeling studies including electron transport and loss processes are required.

Understanding the dynamics of the ring current electron population is a challenging task since the electron distribution significantly depends not only on time and radial coordinate, as it is for the radiation belts, but also on magnetic local time (MLT). Multispacecraft measurements covering different MLT sectors are therefore required to observe the electron population in its global evolution. However, measuring this electron population is complicated by different external effects such as surface charging and contamination by

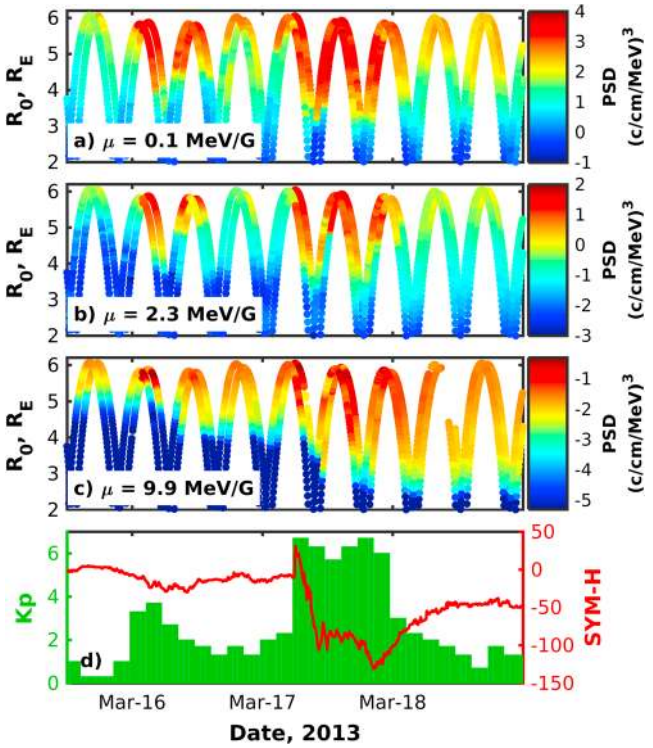

Figure 1. (a–c) Electron PSD derived from the Van Allen Probe observations for $\mu = 0.1, 2.3$, and 9.9 MeV/G and $K = 0.3$ G$^{1/2}R_E$ during the 17 March 2013 storm. (d) The *Kp* (green) and *SYM-H* (red) indices. PSD = phase space density.

photoelectrons and penetrating radiation (see Denton et al., 2017, and references therein). Numerical modeling helps us gain insight into the dynamics of ring current electrons under the scarcity of satellite measurements.

In recent years, a number of ring current models have been developed (e.g., RCM [Chen et al., 2015; Lemon et al., 2004; Toffoletto et al., 2003], RAM [Jordanova et al., 1996, 2016; Jordanova & Miyoshi, 2005], CIMI [Fok et al., 2014, 2011, 1999], IMPTAM [Ganushkina et al., 2013, 2015, 2014], and HEIDI (Ilie et al., 2012; Liemohn et al., 2001). The models include the ring current electron population and typically take into account the processes, which are important for the electron dynamics, such as global convection, localized particle injections, radial diffusion due to drift resonance with ultralow frequency waves, and local scattering rates of the electrons. All models face similar challenges in describing the dynamics of the electrons. Due to the complexity of the system, it is often difficult to analyze model errors. For instance, the underestimation of observed particle fluxes can be driven by overestimated scattering rates as well as unrealistic transport processes or by the combination of both factors. Such model errors are the main hindrance for understanding which physical processes are responsible for the dynamics of the ring current electrons.

In this study, we use the four-dimensional Versatile Electron Radiation Belt (VERB-4D) code (Aseev et al., 2016; Shprits et al., 2015) to understand the mechanisms that control transport and loss of ring current electrons within GEO during the 17 March 2013 storm. By varying different model parameters, we examine the sensitivity of the model and determine the most significant processes that drive the electron transport and loss. To validate the model, we compare simulation results with the Van Allen Probe measurements.

The manuscript is organized as follows. In section 2, we present Van Allen Probe measurements during the 17 March 2013 storm. We describe the modeling approach in section 3. We show simulation results and study the sensitivity of the code in section 4. In section 5, we discuss the results, and the main conclusions of the study are summarized in section 6.

2. Observations of the 17 March 2013 Storm

We use the combined Van Allen Probe Helium, Oxygen, Proton, and Electron (HOPE) mass spectrometer (Funsten et al., 2013) and Magnetic Electron Ion Spectrometer (MagEIS; Blake et al., 2013) Level 3 particle data during the 17 March 2013 geomagnetic storm to calculate electron phase space density (PSD) as a function of the first and second adiabatic invariants μ and K. The HOPE and MagEIS data match up well during the storm (e.g., see supporting information Figure 1 illustrating electron flux spectrum during the storm), and we have not performed an additional intercalibration between the instruments. The apogee of the satellites is located at ~1 hr MLT, and an inbound satellite pass traverses the postmidnight and prenoon MLT sectors, while an outbound pass crosses postnoon and premidnight sectors. We use T04S (Tsyganenko & Sitnov, 2005) magnetic field model incorporated into the IRBEM library (Boscher et al., 2012) to calculate invariants μ and K from observed local pitch angles and energies. To determine values of μ, we also use magnetic field measurements made by Electric and Magnetic Field Instrument Suite and Integrated Science (Kletzing et al., 2013) aboard the satellite. Since values of μ and K vary along the satellite trajectory, we use bilinear interpolation to calculate PSD for given constant μ and K.

Figures 1a–1c show 5-min-averaged electron PSDs, which are obtained from the data for the first adiabatic invariant $\mu = 0.1, 2.3$, and 9.9 MeV/G and second invariant $K = 0.3$ G$^{1/2}R_E$ during the 17 March 2013 storm. The chosen values of the invariants approximately correspond to energies 0.3, 9, and 30 keV at GEO and 1, 30, and 100 keV at $L = 4$ (see Figure 2 illustrating energy and pitch angle dependence on the L shell). The corresponding pitch angles vary from ~ 34° at GEO to 40° at $L = 3$, which ensures that Van Allen

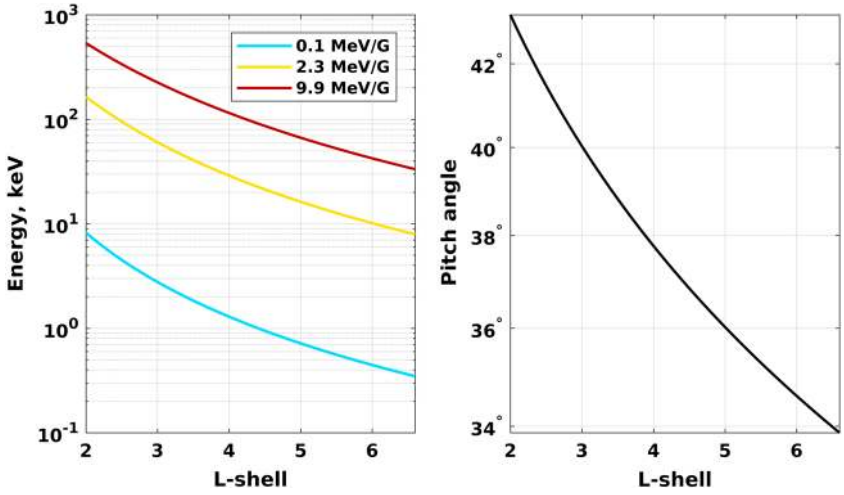

Figure 2. Energies and pitch angles corresponding to different values of the first adiabatic invariant μ. The second invariant $K = 0.3\ \mathrm{G}^{1/2}R_E$ is constant. The energies and pitch angles are calculated using the dipole field.

Probe data are available even if the satellite is significantly off the geomagnetic equator, which can happen during active times.

The geomagnetic storm was driven by a coronal mass ejection that hit the Earth's magnetosphere at 6:00 (see Lyons et al., 2016, for more details). In response to the storm, the *Kp* index (Figure 1d) showed values above 6− for 18 hr, and *SYM-H* index (Figure 1d) reached −130 nT, indicating significant enhancement of the ring current. Ring current electrons were injected down to $R_0 = 2.5$–$3\ R_E$, showing the increase in the PSD until the main phase of the storm ended on ~18 March (see Figures 1a–1c). We note that R_0 denotes here the distance from the center of the Earth to the point of the minimum magnetic field found along the field line at which the spacecraft resides (for this, we used Olson & Pfitzer, 1977, and IGRF; Thébault et al., 2015, magnetic field models). The recovery phase was characterized by the sharp decrease in 0.1 and 2.3 MeV/G electron PSD and a more gradual decrease in 9.9 MeV/G electron PSD.

Although the storm time dynamics of electrons for considered values of μ and K may look similar, it can be driven by different energy-dependent mechanisms. Particles with a half-drift period longer than the main phase of the storm have direct convective access to the ring current region (Lyons & Williams, 1980). The higher-energy particles have shorter drift periods and more efficiently interact with electric field fluctuations, which lead to the inward displacement driven by radial diffusion (Cornwall, 1968; Lyons & Schulz, 1989). Lyons and Schulz (1989) showed that particles with energies $\gtrsim$40 keV are closer to diffusive access, while $\lesssim$40-keV particles have convective access.

The calculated PSD may depend on the used magnetic field model since the calculation of the invariant K requires an integration along a field line that crosses the spacecraft location. Errors in the field model may lead to the uncertainties in the computed PSD. To study the effects of different magnetic field models, we also calculated PSD, using the Tsyganenko (1989; T89), Tsyganenko (1995; T96), Tsyganenko (2002; T01S), and Tsyganenko and Sitnov (2007; TS07D) models.

Figure 3 shows the calculated PSD profiles as a function of R_0 for three consecutive Van Allen Probe B passes during the main phase of the storm. For the first satellite pass beginning at 9:00 on 17 March, the magnetic field models have almost no effect on $\mu = 0.1$ and 9.9 MeV/G electron PSD, while a small difference in PSD is observed for 2.3 MeV/G particles between ~4.6 and 5.3 R_E. For the next pass beginning at 13:30, the PSD profiles, which were calculated using T89, T01S, T04S, and TS07D models slightly differ above ~4.8 R_E for all values of the first invariant, and the T96 model results in generally lower PSD, which are up to 1 order of magnitude smaller than the profiles calculated using the TS07D model. The PSD values along the following pass at 18:00 show insignificant differences for all profiles. As will be shown later, the differences in the PSD obtained from the Van Allen Probe measurements are much smaller than the uncertainties in the numerical model of the ring current electrons, and the errors that the T04S model introduces can be neglected, given a much larger model uncertainty.

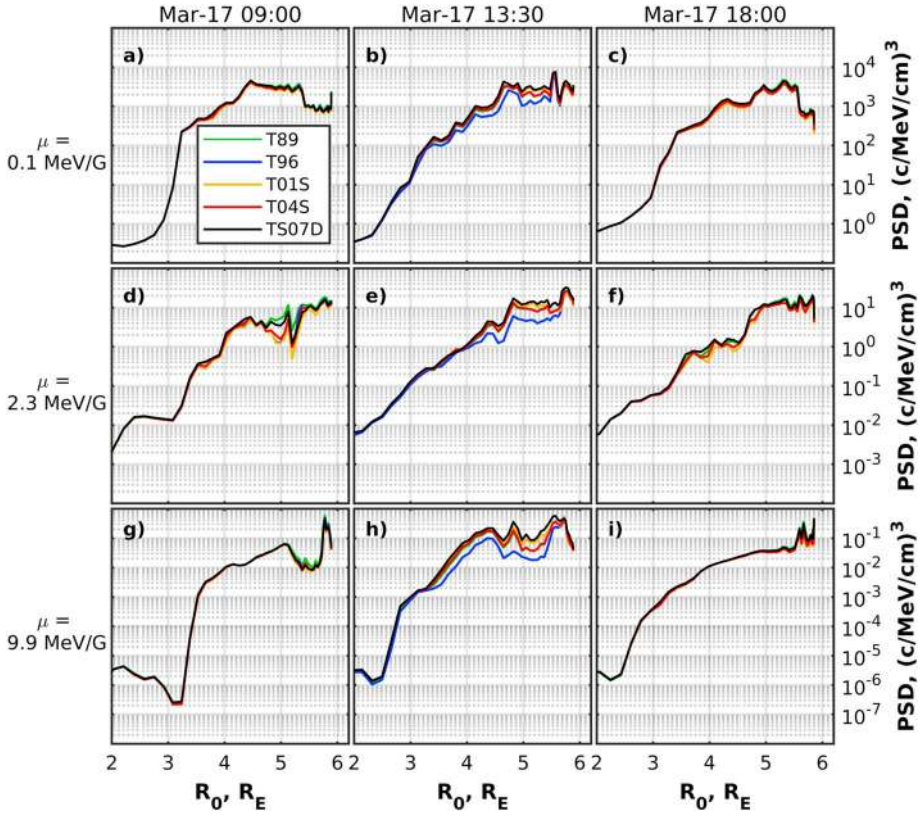

Figure 3. Profiles of electron PSD for $K = 0.3$ G$^{1/2}R_E$ and $\mu = 0.1$ MeV/G (a–c), 2.3 MeV/G (d–f), and 9.9 MeV/G (g–i) calculated using different magnetic field models for three subsequent Van Allen Probe B passes. Columns correspond to the passes beginning at 9:00, 13:30, and 18:00 on 17 March (from left to right). PSD = phase space density.

3. Model Description

We use the VERB-4D code to model the dynamics of the ring current electrons. The code solves the modified Fokker-Planck equation with additional advection terms (Aseev et al., 2016; Shprits et al., 2015). It allows simultaneously modeling ring current and radiation belt dynamics by combining electron drift, radial diffusion, pitch angle and energy diffusion, and loss processes that can be parameterized with the lifetime τ (e.g., magnetopause shadowing is accounted by setting up τ to one-half drift period and loss to the atmosphere is accounted by setting up the lifetimes within the loss cone to one-fourth bounce time):

$$\frac{\partial f}{\partial t} = -\langle v_\varphi \rangle \frac{\partial f}{\partial \varphi} - \langle v_{R_0} \rangle \frac{\partial f}{\partial R_0} + \frac{1}{G}\frac{\partial}{\partial L^*} G \langle D_{L^*L^*} \rangle \frac{\partial f}{\partial L^*} + \\ + \frac{1}{G}\frac{\partial}{\partial V} G \left(\langle D_{VV} \rangle \frac{\partial f}{\partial V} + \langle D_{VK} \rangle \frac{\partial f}{\partial K} \right) + \frac{1}{G}\frac{\partial}{\partial K} G \left(\langle D_{KV} \rangle \frac{\partial f}{\partial V} + \langle D_{KK} \rangle \frac{\partial f}{\partial K} \right) - \frac{f}{\tau}, \quad (1)$$

where f is the PSD; t represents time; φ is MLT, R_0 is the radial distance to a given point in the geomagnetic equator; V, K, and L^* are modified adiabatic invariants (Subbotin & Shprits, 2012); $V = \mu \cdot (K + 0.5)^2$; μ is the first adiabatic invariant; τ is electron lifetime related to scattering into the loss cone and magnetopause shadowing; $\langle v_\varphi \rangle$ and $\langle v_{R_0} \rangle$ are bounce-averaged drift velocities; $\langle D_{L^*L^*} \rangle$, $\langle D_{VV} \rangle$, $\langle D_{VK} \rangle$, $\langle D_{KV} \rangle$, and $\langle D_{KK} \rangle$ are bounce-averaged diffusion coefficients; $G = -2\pi B_0 R_E^2 \sqrt{8 m_0 V}/(K + 0.5)^3/L^{*2}$ is the Jacobian of the coordinate transformation from adiabatic invariants (μ, J, Φ) to (V, K, L^*) (Subbotin & Shprits, 2012), B_0 is the field at the equator at the Earth's surface; and m_0 is electron rest mass.

The VERB-4D code has been designed to simplify the implementation of the most important physical processes responsible for the electron dynamics, and it allows us to efficiently perform ensemble simulations or study sensitivity of the code to different input parameters. The numerical schemes implemented in the

code have been thoroughly tested (Aseev et al., 2016), and it is guaranteed that the numerical errors do not affect the physical interpretation of the results.

The spatial boundaries are set up at $R_0 = 1$ and 6.6 R_E, with 0.5-hr and 0.2-R_E grid steps in MLT and radial distance, respectively. To construct a grid in V and K, we create a logarithmic grid in energy and pitch angles limited by 200 eV and 30 keV and 0.7° and 89.3° at GEO with 60 nodes in energy and 61 nodes in pitch angle. Adiabatic invariants are then calculated on this grid, using the dipole field model. We choose these energy limits at GEO to fit in the statistical boundary condition model described below.

To model the enhancement of PSD during the main phase of the storm, we set up initial conditions from Van Allen Probe B inbound pass starting at 20:00 on 16 March and ending at midnight on 17 March. We use PSD derived from HOPE and MagEIS measurements, assume symmetry in MLT, and assign the calculated initial conditions to 20:00 16 March. Boundary conditions in MLT are periodic. At the lower boundary $R_0 = 1$ R_E, we assume zero PSD since all particles are lost in the atmosphere. To specify the outer boundary at $R_0 = 6.6\,R_E$, we use the statistical model of electron fluxes developed by Denton et al. (2016). The model is based on 82 satellite years of observations at GEO made by magnetospheric plasma analyzer instruments onboard Los Alamos National Laboratory satellites. The model provides spin-averaged electron fluxes as a function of energy, MLT, and the *Kp* index and covers the energy range from ~40 eV to 40 keV at GEO. Along with the mean and median values of the fluxes, 5th, 25th, 75th, and 95th percentile limits are also given. To obtain directional flux from the spin-averaged flux, we assume its sinusoidal dependence on the pitch angle.

We take into account electron scattering driven by hiss and chorus waves by using parameterized electron lifetimes included in the parameter τ instead of local diffusion terms (fourth and fifth terms on the right-hand side of equation (1)). In this case, boundary conditions in the invariants V and K are not required since there is no feedback from local diffusion terms. We use the MLT-averaged model of electron lifetimes within the plasmasphere developed by Orlova et al. (2016). Outside the plasmasphere, we utilize the MLT-dependent scattering rates obtained by Gu et al. (2012). The plasmapause location is calculated using the Carpenter and Anderson (1992) model.

We use the realistic T89 mangetic field model and the Weimer (2005; W05) polar cap potential model to calculate electron $E \times B$ and gradient-curvature drift velocities at the geomagnetic equator. The polar cap potential is mapped along the equipotential dipole field lines down to the geomagnetic equator. At the equator, the electric field is numerically calculated, using a central differencing scheme (we refer to the calculated electric field as W05 electric field model). Compared to the commonly used *Kp*-driven Volland-Stern electric field model, the W05 model is parameterized with solar wind parameters, which ensures more realistic variability of the global electric field, naturally driven by the dayside reconnection. In the current work, we feed 15-min-averaged solar wind parameters to the W05 model.

We utilize *Kp*-parameterized radial diffusion rates by Brautigam and Albert (2000). We note that similar results are obtained with Ozeke et al. (2014) parameterization. To simultaneously account for the direct convective access and diffusive access of electrons to the ring current region, we smoothly zero out the diffusion rates for electron energies smaller than the threshold of 40 keV proposed by Lyons and Schulz (1989).

4. Results

In this section, we show the results of the VERB-4D code and compare them with the PSD calculated along the Van Allen Probes trajectories. We present the confidence intervals of the model, which are associated with the uncertainties in the outer boundary conditions. We also study the sensitivity of the results to the input parameters such as convection electric field, electron loss rates, radial diffusion coefficients, and SAPS electric fields.

We start all simulations that are presented in this section at 20:00 on 16 March 2013 with a time step of 15 min. We stop the simulations at 00:00 on 18 March 2013 to model the storm time enhancement of PSD across a given range of energies. We then interpolate the global distribution of PSD provided by the VERB-4D code along the Van Allen Probe trajectories, using linear interpolation in time, radial distance, and MLT. The target values of μ and K invariants to compare with satellite data were chosen to match the corresponding grid values of the VERB-4D code.

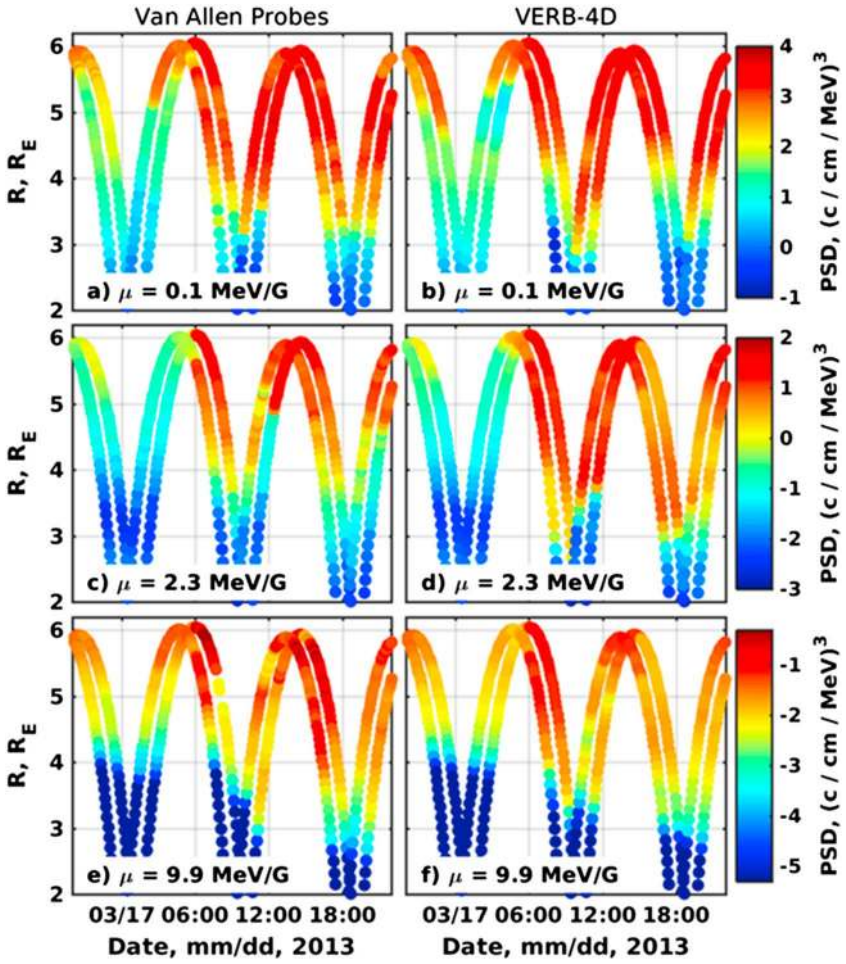

Figure 4. Comparison of the Van Allen Probe PSD (left column) with the VERB-4D code results (right column) for $\mu = 0.1$, 2.3, and 9.9 MeV/G and $K = 0.3$ G$^{1/2}R_E$. The figure represents an in situ comparison, made at the location of the spacecraft. The mean boundary flux is used. A leftmost orbit along a given inbound or outbound pass corresponds to the Van Allen Probe B trajcetory. PSD = phase space density; VERB-4D = four-dimensional Versatile Electron Radiation Belt.

4.1. Model-Data Comparison Along the Van Allen Probe Orbits

We use the mean value of the Denton et al. (2015) statistical flux distribution and the W05 electric field to model the storm time dynamics of the ring current electrons. Other input parameters are the same as described in section 3.

Figure 4 shows the comparison between the Van Allen Probe data and the results of the VERB-4D code for $\mu = 0.1$, 2.3, and 9.9 MeV/G and $K = 0.3$ G$^{1/2}R_E$ electrons. The leftmost orbit along a given inbound or output pass in Figure 4 corresponds to the Van Allen Probe B trajectory since the Van Allen Probe B moves ahead of the Van Allen Probe A for the chosen time interval.

The storm time dynamics of the 0.1 MeV/G electrons (Figure 4a) is reproduced relatively well by the VERB-4D code (Figure 4b). The code captures the time and radial extent of the PSD enhancement. The measurements along the pass starting at 6:00 on 17 March 2013, just before the storm onset, show the increase in electron PSD from ~6 R_E to as low as 3.5–4 R_E, and the code is able to reproduce the increase, predicting the radial extent of the enhancement ~0.1–0.2 R_E farther away from the Earth than it is seen in the data. In agreement with the data, the model results show the earthward penetration of the electrons along the next satellite pass at ~9:00 down to 3 R_E for Van Allen Probe B and to 3.5 R_E for the Van Allen Probe A. For the next two passes, the model agrees well with the observations between ~4 R_E and 6 R_E and generally underestimates PSD between 3 and 4 R_E.

The comparison between the code and the data for $\mu = 2.3$ and 9.9 MeV/G electrons between ~6:00 and 10:00 reveals an interesting fact that the enhancements in the modeled PSD extend closer to the Earth than the data show, while the code agrees well with the data for $\mu = 0.1$ MeV/G electrons. The increase in 2.3 MeV/G PSD is observed down to ~4 R_E (Figure 4c), and the code predicts higher PSD between 3 and 4 R_E (Figure 4d). The observed enhancement in 9.9 MeV/G electron PSD extends down to 4.5–5 R_E (Figure 4e) for the same time interval, while the enhancement in the code spreads down to 3.5–4 R_E (Figure 4f). Such a mismatch in the model predictions between 0.1 MeV/G and higher-energy electrons can be explained by the strong convective electric field or shorter lifetimes of the 0.1 MeV/G electrons, which are implemented in the model.

For the outbound satellite pass between ~10:00 and 13:00, the code overestimates the observations for $\mu = 2.3$ MeV/G electrons from ~3.5 to 4.9 R_E, which can be due to the stronger earthward propagation that occurred during the previous pass. We note that the Van Allen Probe A shows the sudden increase in electron PSD at 4.9 R_E occurred at 12:00, as the satellite moves to the apogee. Such an increase cannot be attributed to the energy boundary between HOPE and MagEIS instruments since the boundary is located at ~3.2 R_E for the given first and second adiabatic invariants. The nature of the increase is not clear since the Van Allen Probe B traversing similar region shows much higher PSD between 4 and 4.9 R_E than the Van Allen Probe A observes. The model overestimates PSD between 3 and 4.5 R_E along the next two satellite passes after 13:00 and agrees better at higher radial distances.

The model results for the $\mu = 9.9$ MeV/G particles matches well the observations between 3 and 4 R_E after 10:00 despite the overestimated PSD at the previous satellite pass. Above 4 R_E, the model generally shows slightly lower PSD values than observed in the data.

The results presented in this section indicate that the model is capable of qualitatively and quantitatively reproducing the dynamics of the ring current electron population above 4.5 R_E. The model can capture the features of the enhancements in that region, although the magnitude of PSD may slightly differ from the observations. The differences between the model and data above 4.5 R_E can be explained by the simplified *Kp*-dependent model of the spatial outer boundary conditions. Below 4.5 R_E, the discrepancies between the model and the data are generally higher, which can be indicative of the uncertainties in electric and magnetic fields or in electron lifetimes. In the next sections, we study the discrepancies between the model and the data in more detail by analyzing the sensitivity of the code to the input parameters.

4.2. Sensitivity to the Outer Boundary Conditions

To study the sensitivity of the model to the boundary conditions and provide approximate confidence interval of the model, we perform simulations with 5th, 25th, 75th, and 95th percentiles of statistical distribution of electron flux at GEO (Denton et al., 2015), keeping all other input parameters the same as in section 4.1. Figure 5 presents PSD profiles for $\mu = 0.1$, 2.3, and 9.9 MeV/G and $K = 0.3\ \mathrm{G}^{1/2}R_E$ together with percentile limits for three subsequent Van Allen Probe B passes starting at 9:00 on 17 March. The figure shows that most of the time satellite data are within the percentile limits, generally showing better agreement above $R_0 = 3.5\ R_E$ across all adiabatic invariants. Note that PSD varies by up to 4 orders of magnitude and the model covers rather well this variability within the confidence interval. Below 3.5 R_E, $\mu = 0.1$ MeV/G electron PSD profiles diverge from simulation results, demonstrating deeper earthward displacement by approximately 0.3 R_E for the satellite pass that started at 9:00 (Figure 5a) and lower PSD values for the next pass (Figure 5b), underestimating the inner boundary by approximately 0.3 R_E. The results for 2.3 MeV/G electrons are generally higher than the data for the first two presented satellite passes between 3 and 4 R_E, yet the satellite observations show much better agreement at others radial distances. The values and shapes of PSD profiles for $\mu = 9.9$ MeV/G are very close to the 25th and 75th percentile limits across all radial distances.

Although the magnitude of the modeled PSD depends on the outer boundary conditions that are used in the simulations, the shape of the profiles remains mostly unchanged. This fact does not necessarily imply that the boundary conditions have no effect on the shape of the profiles or the observed smaller-scale features. Since we use different percentile values of the electron flux at GEO as the boundary conditions, the increase or decrease in the magnitude of the boundary conditions takes place along all MLT sectors at the same time. The percentile values, thus, provide approximate lower and upper limits of the PSD magnitude and do not affect the shape of the profiles.

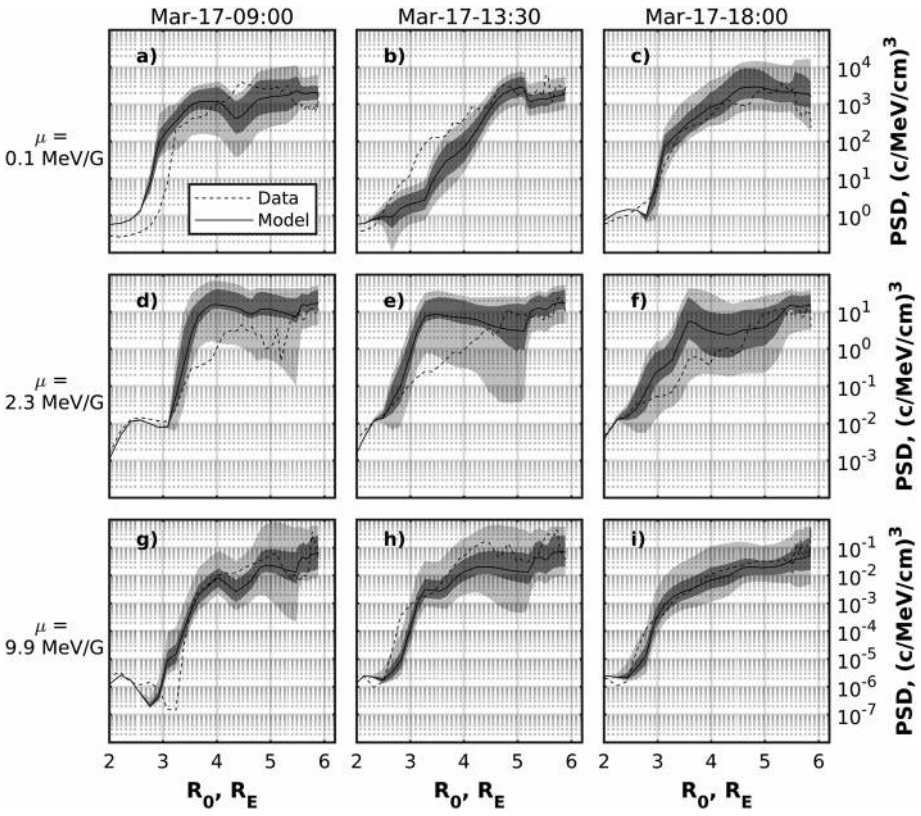

Figure 5. Comparison between Van Allen Probe B data (dashed lines) with the VERB-4D code results (solid lines) for $K = 0.3\ G^{1/2}R_E$ and $\mu = 0.1$ MeV/G (a–c), 2.3 MeV/G (d–f), and 9.9 MeV/G (g–i). Columns correspond to satellite passes beginning at 9:00, 13:30, and 18:00 on 17 March (from left to right). The dark gray regions are limited by the 25th and 75th percentiles of the outer radial boundary conditions. The light gray regions are limited by the 5th and 95th percentiles. PSD = phase space density.

The fact that the Van Allen Probe observations do not fit in the 5th and 95th percentile limits indicates that the discrepancies between the model and data, which is evident in Figure 5a below 3 R_E and in Figures 5b and 5e between 3 and 4 R_E, are most probably caused by other model parameters such as electric field or electron loss rates.

4.3. Role of the Electric Field Model

The differences between the observed PSD and the results of the VERB-4D code (e.g., see Figure 4) can partially stem from the inaccuracies of the electric field model. In this section, we study the role of the global electric field in the simulations.

Figure 6 presents the comparison between the local electric field measured by the Van Allen Probe Electric Field and Waves (EFW) instrument (Wygant et al., 2013) and the W05 electric field model interpolated in time and space along the satellite trajectory. The presented electric fields are in a reference frame corotating with the Earth. We use 6-min moving average of the observed electric fields. We eliminate intervals when spacecraft charging affects the measurements and when the satellites reside in the Earth's shadow and observations are compromised. Figure 6 shows the measured E_y component in the MGSE coordinate system (Wygant et al., 2013) and the E_y component in GSE system obtained from the W05 model. The MGSE system has been developed to isolate the more accurately measured components of the electric field, and the Y-axis in GSE system is most nearly aligned with the Y-axis in MGSE system.

The W05 electric field is similar to the Van Allen Probe observations between ~6:00 and 8:00 on 17 March 2013, slightly overestimating the measurements. When the Van Allen Probe A moves toward perigee, it observes an increase in the electric field magnitude from 8:00, when the spacecraft is at 5 R_E, to ~9:30, when the spacecraft resides at 3 R_E. The W05 model also predicts an increase in the electric field, but the model shows a distinct peak at 9:00 (~ 3.5 R_E) that is ~3.5 times higher than observed electric field (Figure 6a).

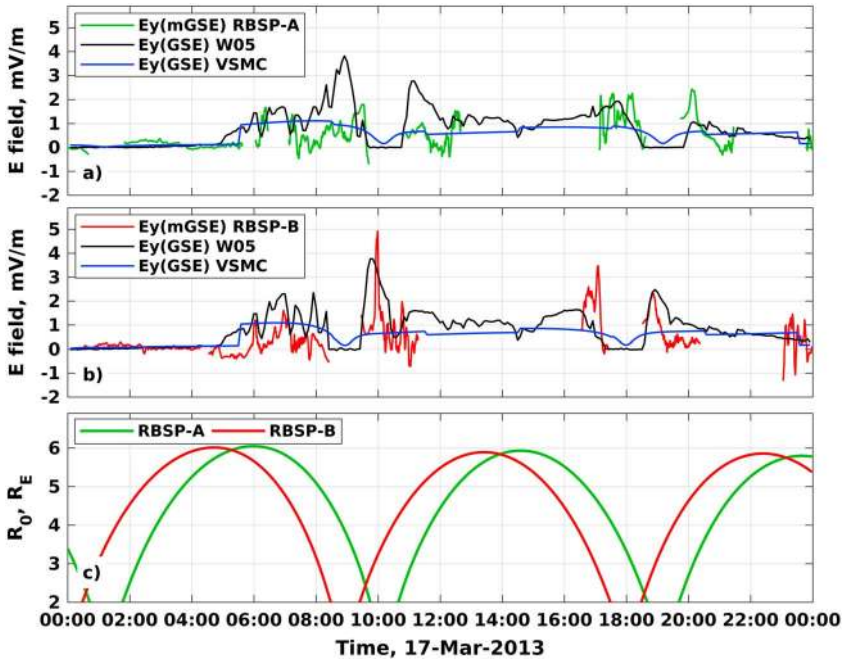

Figure 6. (a, b) Comparison between electric fields measured by the Van Allen Probes A and B (green and red lines), the Weimer (2005) electric field model (black lines), and the VSMC electric field model (blue lines). The electric fields are presented in the reference frame corotating with the Earth. The model electric fields are calculated along the satellite trajectories. (c) The Van Allen Probe R_0 (the distance from the center of the Earth to the point of the minimum magnetic field along the magnetic field line crossing the spacecraft location). VSMC = Volland, (1973), Stern, (1975), and Maynard and Chen (1975); RBSP = Radiation Belt Storm Probes; GSE = geocentric solar ecliptic; mGSE = modified GSE.

The W05 electric field at the next satellite pass also shows a peak at the same location. The Van Allen Probe B shows a similar enhancement at ~10:00, which is, however, more narrow than the W05 model predicts (see Figure 6b). Overall, the model electric field noticeably overestimates the measurements between 8:00 and 10:00. Such an overestimation can explain the fact that the model results are higher than the data for 2.3 and 9.9 MeV/G particles below 4-4.5 R_E along the inbound satellite pass beginning at 6:00 (see Figure 4).

To understand how the global electric field can affect simulation results, we perform a simulation, using the *Kp*-dependent Volland-Stern electric field model (Volland, 1973; Stern, 1975; Maynard & Chen, 1975 [VSMC]) and keep all other parameters the same as in section 4.1. The comparison of the VSMC electric field with the EFW measurements is shown in Figure 6. Since the *Kp* index reaches ~6 and stays approximately constant for 18 hr, the VSMC model shows almost no variations which are constantly seen in the data. Compared to the W05 model, the E_y component of the VSMC electric field is mostly lower, and the models agree better at higher radial distances.

Figure 7 presents the comparison of the resulting PSD for μ = 0.1, 2.3, 9.9 MeV/G and K = 0.3 $G^{1/2}R_E$ electrons interpolated along the Van Allen Probe B trajectory for different electric field models. The electric field models have almost no effect on the profiles of 9.9 MeV/G electrons, due to the gradient and curvature drifts, which are relatively strong for these particles. The magnitude of 0.1 and 2.3 MeV/G electron PSD for W05 and VSMC electric field models are very similar above ~4.5 R_E. This result is consistent with Figure 6 showing that both electric field models do not differ much at higher radial distances. Below 4.5 R_E, where the VSMC electric field are much smaller than the W05 field, the electron profiles obtained with the VSMC model are significantly lower compared to the profiles obtained with the W05 model. The VSMC electric field model leads to larger differences in 0.1 and 2.3 MeV/G electron PSD profiles and data between ~2.5 and 4–4.5 R_E. We note a peak in the 0.1 MeV/G profiles that is observed near 3 R_E, which can be formed due to a stronger loss and slow earthward transport from GEO if the VSMC model is used.

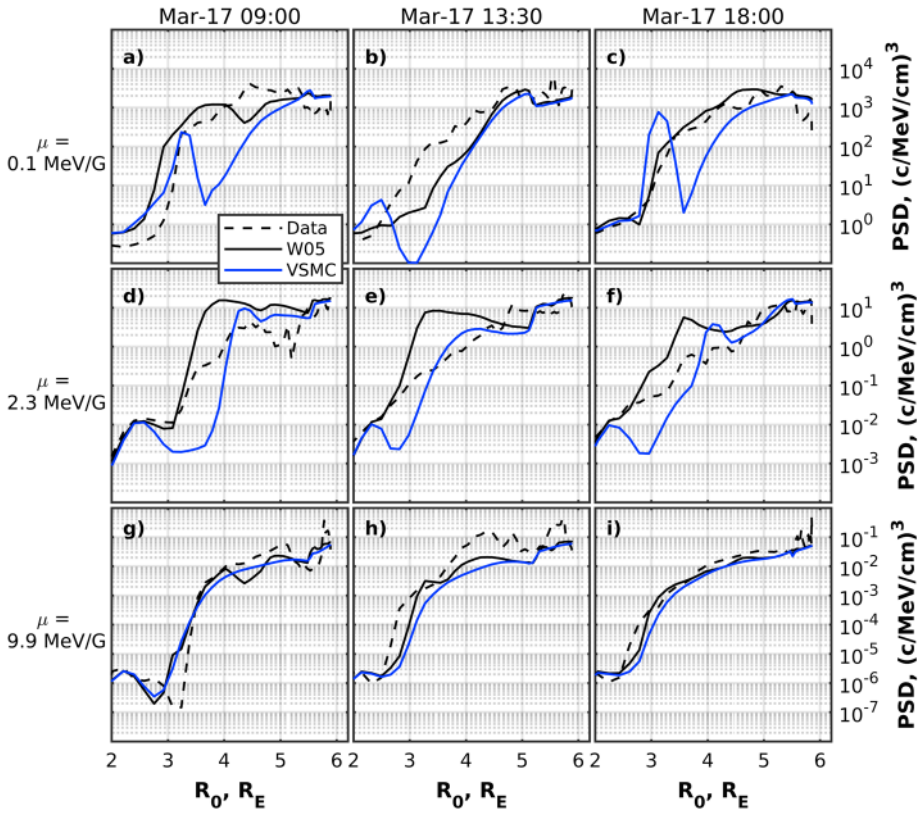

Figure 7. Comparison between the Van Allen Probe B PSD (dashed lines) with the VERB-4D code results if the W05 electric field model is used (black solid line) and if the Volland, (1973), Stern, (1975), and Maynard and Chen (1975) electric field model is used (blue solid lines) for $K = 0.3$ G$^{1/2}R_E$ and $\mu = 0.1$ MeV/G (a–c), 2.3 MeV/G (d–f), and 9.9 MeV/G (g–i). Columns correspond to satellite passes beginning at 9:00, 13:30, and 18:00 on 17 March (from left to right). PSD = phase space density.

Figures 8 and 9 illustrate the global evolution of the modeled PSD for $\mu = 2.3$ MeV/G and $K = 0.3$ G$^{1/2}R_E$ electrons for different electric field models and several time moments during the main phase of the storm. At 6:00 on 17 March 2013, just before the storm, the PSD obtained with the W05 model show the increase propagating from GEO to ~5 R_E at the nightside (Figure 8a), while the VSMC model only predicts the increase down to ~6 R_E (Figure 9a). In general, the W05 model leads to the propagation of the electrons down to 3 R_E at a later time, up to 1 R_E deeper than in the case of the VSMC model. The enhanced PSD obtained with the W05 model fill the region between 3 and 5 R_E in the MLT sector between 21 and 12 hr from 9:00 to 18:00 (Figures 8b–8e). Such an enhancement is also evident in Figure 5 as a peak in 2.3 MeV/G electron PSD profiles computed with the VERB-4D code. The VSMC model predicts lower PSD in the same region (Figures 9b–9e). Both models give qualitatively and quantitatively similar results above 4.5–5 R_E, in good agreement with the data, as shown in Figure 7. Another region of the difference in the modeled global distributions is around the duskside from 14 to 21 hr MLT. This region contains the stagnation point that separates open and closed drift paths, and the small difference in the electric field model can affect the trapping of particles in the code and potentially lead to the overestimation or underestimation of the measurements. We note that Van Allen Probes do not cross this region during the considered event, and the difference in the dynamics there have to be addressed in future studies.

4.4. Sensitivity to the Electron Lifetime Model

In this section, we study the sensitivity of the code results to the electron lifetime model. We perform several simulations with the same model parameters as described in section 4.1 and vary the electron lifetimes outside the plasmasphere. We multiply and divide the lifetimes by 2 and 10, and if the lifetimes are lower than the strong diffusion limit predicts, we assume the strong diffusion approximation.

Figure 10 presents the resulting profiles interpolated along the Van Allen Probe B trajectory for different electron lifetimes. The $\mu = 0.1$ MeV/G profiles are the most sensitive to the changes in the lifetimes. The

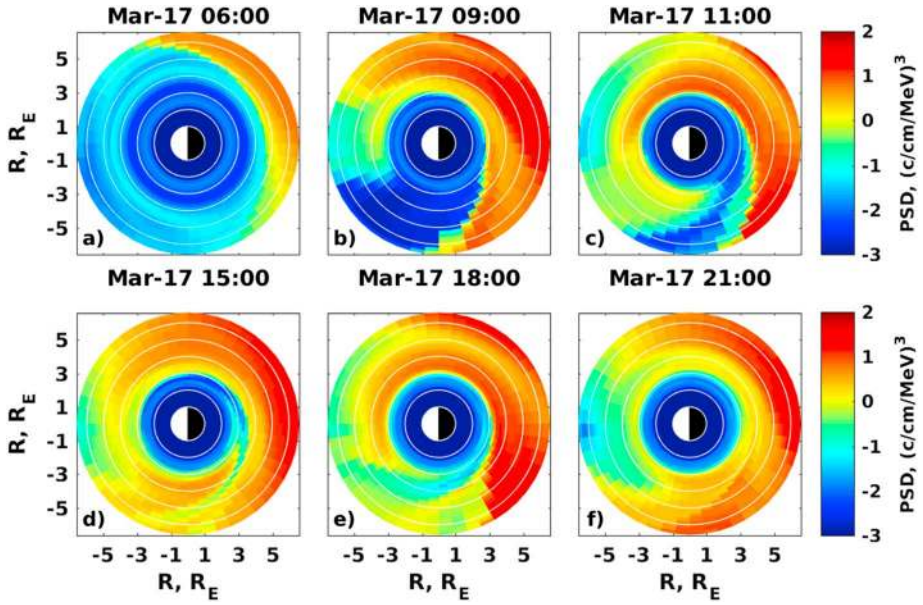

Figure 8. Global PSD distribution of $\mu = 2.3$ MeV/G and $K = 0.3$ G$^{1/2}R_E$ electrons obtained with VERB-4D code if the Weimer (2005) electric field model is used. PSD = phase space density.

twofold increase or decrease in the lifetimes may lead to the difference in PSD larger than 1 order of magnitude and different shape of the profiles (e.g., Figure 10b). The $\mu = 2.3$ MeV/G profiles are less sensitive to the increase in the electron lifetimes (Figures 10d–10f), while the profiles differ more significantly if the lifetimes are decreased. The twofold decrease in the lifetimes results in similar shape and magnitude of the profiles, while the tenfold decrease leads to unrealistically low model results. The profiles of $\mu = 9.9$ MeV/G particles are not noticeably changed due to the increase and twofold decrease in electron lifetimes, and the tenfold decrease in electron lifetimes produces results much smaller than the data. The model results are generally less sensitive to the electron lifetimes above 4.5 R_E for all μ values, while the difference between the simulations grows with decreasing radial distance.

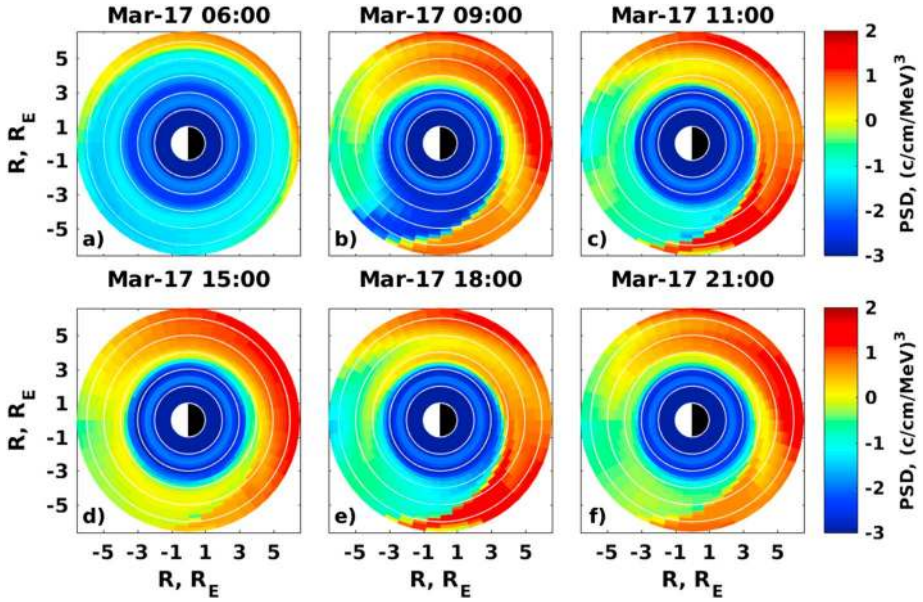

Figure 9. Global PSD distribution of $\mu = 2.3$ MeV/G and $K = 0.3$ G$^{1/2}R_E$ electrons obtained with the VERB-4D code if the Volland (1973), Stern (1975), and Maynard and Chen (1975) electric field model is used. PSD = phase space density.

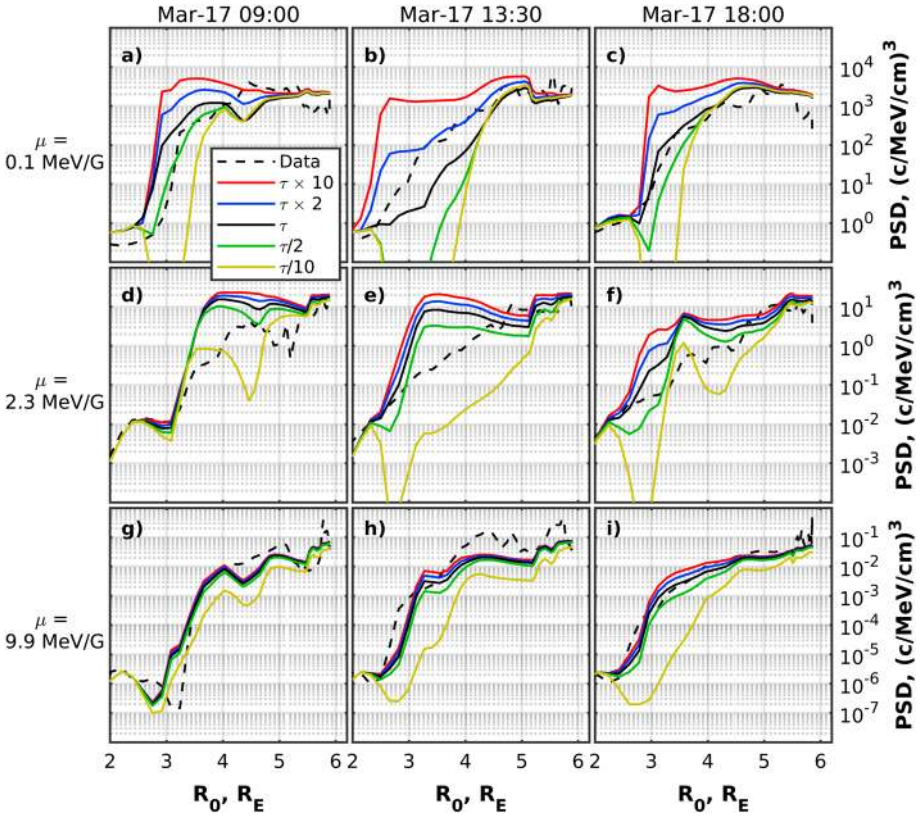

Figure 10. Comparison between the Van Allen Probe B PSD (dashed lines) with the VERB-4D code results for different electron lifetimes outside the plasmasphere (solid lines) for $K = 0.3$ G$^{1/2}R_E$ and $\mu = 0.1$ MeV/G (a–c), 2.3 MeV/G (d–f), and 9.9 MeV/G (g–i). Columns correspond to satellite passes beginning at 9:00, 13:30, and 18:00 on 17 March (from left to right). PSD = phase space density.

4.5. Effects of Radial Diffusion

To demonstrate the role of the radial diffusion, we perform an additional simulation with all input parameters, which have been used in section 4.1 and set up the radial diffusion coefficient $D_{L^*L^*}$ to 0. Figure 11 shows the comparison between the simulations with and without radial diffusion term for $\mu = 9.9$ MeV/G and $K = 0.3$ G$^{1/2}R_E$ electrons. We note that the diffusion coefficient for 0.1 and 2.3 MeV/G electrons is 0 by the setup of the model, and the results of both simulations are identical for these particle populations. The simulation with radial diffusion term agrees better with the data for all considered satellite passes. The

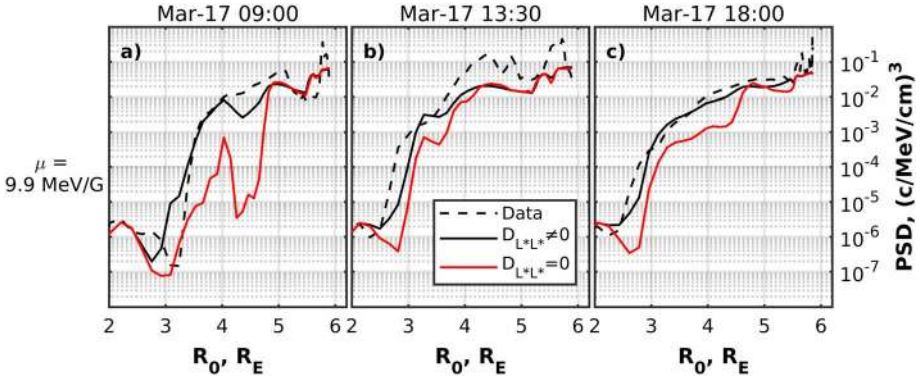

Figure 11. Comparison between the Van Allen Probe B PSD (dashed lines) with the VERB-4D code results with and without radial diffusion term (black and red solid lines, respectively) for $K = 0.3$ G$^{1/2}R_E$ and $\mu = 9.9$ MeV/G electrons. Columns correspond to satellite passes beginning at 9:00, 13:30, and 18:00 on 17 March (from left to right). PSD = phase space density.

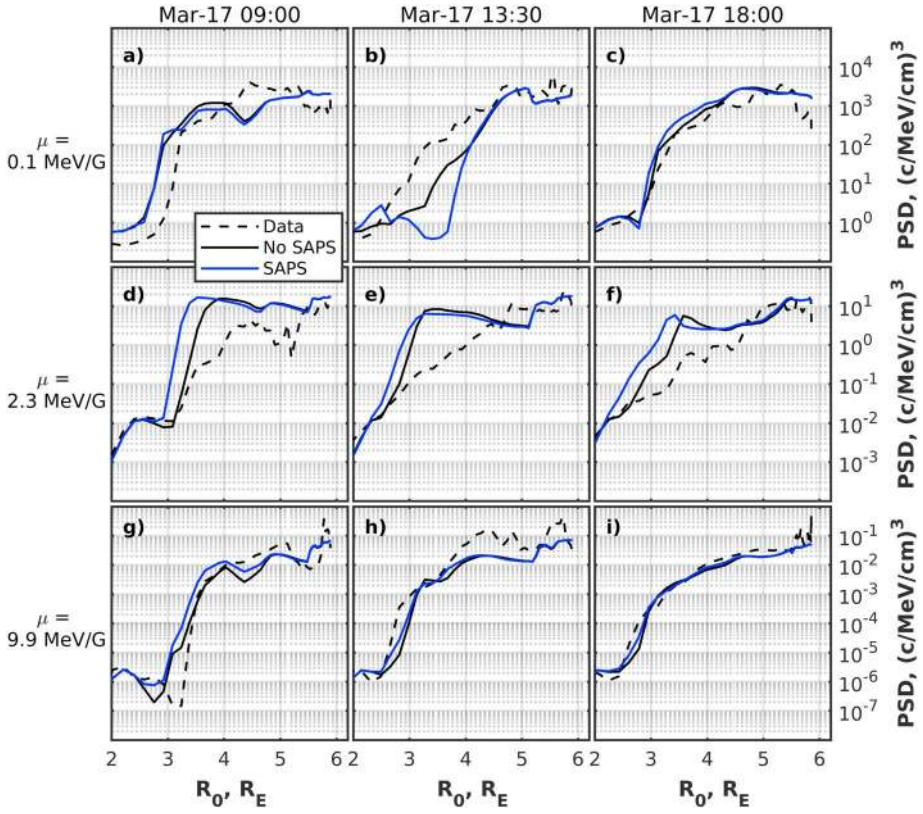

Figure 12. Comparison between Van Allen Probe B data (dashed lines) with the VERB-4D code results with and without subauroral polarization streams included (blue and black solid lines, respectively) for $K = 0.3$ $G^{1/2}R_E$ and $\mu = 0.1$ MeV/G (a–c), 2.3 MeV/G (d–f), and 9.9 MeV/G (g–i). Columns correspond to satellite passes beginning at 9:00, 13:30, and 18:00 on 17 March (from left to right). PSD = phase space density.

difference between the simulations is most evident along a satellite pass starting at 9:00 (Figure 11). The radial diffusion term results in deeper propagation of the PSD profiles compared to the simulation when radial diffusion is not included in the code. The simulations give almost the same results above 4.5 R_E, and the discrepancies are observed at lower radial distances.

4.6. Effects of SAPS

The SAPS electric field can potentially affect the dynamics of the ring current electrons below ~4 R_E. To estimate an effect of SAPS, we performed a simulation with the included *Kp*-dependent model of SAPS, using the approach developed by Goldstein et al. (2005). Figure 12 presents the results in the same format as Figure 7. The overall effect of SAPS is relatively small for $\mu = 9.9$ MeV/G particles. SAPS lead to the deeper earthward propagation of the 2.3 MeV/G electron PSD profiles than the model without SAPS. The difference between two simulations for 0.1 MeV/G electrons is noticeable between 3 and 4 R_E at 13:30 on 17 March 2013, and results obtained with the SAPS model included diverge strongly from the data along this satellite pass (Figure 12b). The implemented model of SAPS have no effect on the shape of the profiles (except the profiles in Figure 12b), leading to a small earthward shift of the PSD profiles. We note that the *Kp*-driven SAPS model creates very slow changes in the electric field, and the effect may be more pronounced with a more variable realistic field.

5. Discussion

The comparison between the VERB-4D code and the Van Allen Probe data demonstrate that the model results are almost insensitive to the input parameters, such as electric field model, electron scattering rates, boundary conditions, radial diffusion, and SAPS model, for $\mu = 0.1$, 2.3, and 9.9 MeV/G and $K = 0.3$ $G^{1/2}$ electrons above ~4.5 R_E. The observed PSD fit in the approximate confidence intervals associated with the uncertainties in boundary conditions and are almost always within the 25th and 75th percentile limits

above 4.5 R_E (see Figure 5). The simulations with the W05 and VSMC electric field models give similar results in that region, with PSD being slightly higher in the case of W05 model (see Figure 7). Between 4.5 R_E and GEO, the code results are almost insensitive to the electron lifetimes, and the SAPS have no effect on the PSD profiles. A good agreement between the model and the observations above 4.5 R_E indicate that realistic boundary conditions that are transported inward by the global-scale electric and magnetic field can generally explain the PSD enhancement in that region. The use of more accurate boundary conditions from the observations as well as localized electric and magnetic fields may help reproduce smaller-scale features observed in the data.

The model results differ from the data more noticeably below 4.5 R_E, and the biggest discrepancies are likely explained by the errors in electric field and electron lifetime models. The in situ comparison between the electric field measured by Van Allen Probes and the field computed with the W05 model shows that the model electric field agrees better with the observations at higher radial distances and overestimates the measurements at lower distances down to as low as 3 R_E at the beginning of the storm (see Figure 6). The unrealistically strong electric field at lower radial distances is a possible reason for the overestimation of electron PSD below 4 R_E for 2.3 and 9.9 MeV/G electrons from 8:00 to 10:00 (see Figure 4). The peak in 2.3 MeV/G electron PSD profiles between 3 and 4 R_E (Figures 5d–5f) is not observed in the data and is most probably caused by the uncertainties in W05 electric field model since the VSMC model leads to the less pronounced peak and even underestimation of the measurements at lower radial distances (see Figures 7d–7f). The 0.1 MeV/G electron PSD profiles are the most sensitive to the electron lifetimes, and the simultaneous overestimation of the observed PSD for 2.3 MeV/G electrons and underestimation for 0.1 MeV/G electrons along the Van Allen Probe B trajectory beginning at 13:30 on 17 March 2013 (Figures 5b and 5e) may be caused by the combined effects of uncertainties in the lifetimes and electric field. We note that tenfold decrease in electron lifetimes leads to unrealistic results for all considered adiabatic invariants.

The quantification of the radial diffusion of the ring current electrons needs to be further investigated in future studies. With regard to the 17 March 2013 storm, the global-scale convection does not reproduce the radial extent of the 9.9 MeV/G profiles below 4–5 R_E, while the inclusion of the radial diffusion term leads to much better agreement with the measurements (see Figure 11). We note here that in general, the radial diffusion is not the only candidate for explaining the dynamics of these particles. For instance, the SAPS electric field can also contribute to their transport. Although the simplest *Kp*-dependent model of the SAPS (Goldstein et al., 2005) that we tested in this study produces only a slight earthward shift of the profiles (Figure 12), more realistic models, including self-consistent treatment of the electric field (Yu et al., 2017), potentially may cause more noticeable effects. The localized particle injections due to penetrating dipolarization fronts can also contribute to the electron radial transport, but their effects are typically observed at higher radial distances.

The use of the local diffusion term and MLT-dependent chorus wave models can further improve the simulation results. Since most of the chorus wave models have been designed for the radiation belts, they assume that the wave amplitude and normal angle distribution do not vary within rather wide day and night MLT sectors (e.g., Agapitov et al., 2015, 2018; Spasojevic & Shprits, 2013). While such an assumption can be justified in three-dimensional radiation belt codes, four-dimensional models of the ring current electrons may require more accurate MLT-dependent chorus wave parameterizations. We also emphasize the importance of the plasmasphere model that separates hiss and chorus wave-driven scattering of electrons. Inaccuracy in the demarcation boundary between the regions dominated by different waves and different plasma conditions introduces additional uncertainty in the simulations. More advanced MLT-dependent models (e.g., derived from neural network-based model of plasmasphere, e.g., Zhelavskaya et al., 2017) will be included in our future studies.

6. Summary

In this study, we modeled the storm time enhancement of ring current electron PSD during the 17 March 2013 storm for $\mu = 0.1$, 2.3, and 9.9 MeV/G and $K = 0.3$ $G^{1/2}R_E$ electrons, which covers the energies from 1 to 100 keV at $L = 4$, using the VERB-4D code. Our model includes magnetospheric convection driven by global magnetic and electric fields, radial diffusion, and electron scattering rates due to interaction with whistler-mode hiss and chorus waves. We compared the simulation results with the Van Allen Probe data and studied the sensitivity of the model to the input parameters including the global electric field, outer

boundary conditions at GEO, electron lifetimes outside of the plasmasphere, radial diffusion, and SAPS. The main conclusions are stated below.

- For the considered event, simulation results are relatively insensitive to all tested input parameters above 4.5 R_E for all considered adiabatic invariants, and the general dynamics of the particles between 4.5 and 6.6 R_E appear to be driven by the transport of the particles from GEO under the action of the global electric and magnetic fields.
- Although the sensitivity of the model to the localized electric fields has not been tested in this study, our results indicate that the discrepancies between the model and data between 4.5 R_E and GEO can be explained by uncertainties in boundary conditions, and additional physical processes, such as the localized fields, may not be needed to reproduce the general evolution of the ring current electrons in that region.
- The main discrepancies between the model and data below 4.5 R_E can be explained by errors in the global electric field and electron lifetimes.
- The global convective transport cannot reproduce the radial extent of the 9.9 MeV/G electron profiles below ~4.5 R_E, and the inclusion of the radial diffusion term with the diffusion rates by Brautigam and Albert (2000) leads to better agreement with the data.
- The *Kp*-driven SAPS model (Goldstein et al., 2005) leads to relatively small changes in the electron profiles, which seem to be less significant than the uncertainties related to lifetimes or electric field.

This study presents the initial step toward understanding the complicated transport and loss processes of low-energy electrons within GEO. The future extension of this study will include modeling of lower-energy electrons, improvement of the loss and fields model, and understanding of the contribution of localized electric fields beyond and inside GEO.

Acknowledgments
The authors acknowledge use of NASA/GSFC's Space Physics Data Facility's OMNIWeb service, and OMNI data. The *Kp* index was provided by GFZ Potsdam. The authors are grateful to the RBSP-ECT team for the provision of Van Allen Probes observations. All RBSP-ECT data are publicly available at the web site http://www.RBSP-ect.lanl.gov/. This research was supported by the Helmholtz-Gemeinschaft (HGF; http://10.13039/501100001656), NASA grants NNX15AI94G and NNX16AG78G, NSF grant AGS-1552321, and project PROGRESS funded by EC | Horizon 2020 Framework Programme (H2020; http://10.13039/100010661; 637302). The research has been partially funded by Deutsche Forschungsgemeinschaft (DFG) through grant CRC 1294 Data Assimilation, Project B06. Processing and analysis of the ECT data was supported by Energetic Particle, Composition, and Thermal Plasma (RBSP-ECT) investigation funded under NASA's Prime contract NAS5-01072. The work by the EFW team was conducted under JHU/APL contract 922613 (RBSP-EFW). This work used computational and storage services associated with the Hoffman2 Shared Cluster provided by UCLA Institute for Digital Research and Education's Research Technology Group. The authors thank the developers of the IRBEM library, which was adapted for use in the current study and Daniel Weimer for the provision of the codes for global electric field model. The authors are grateful to Sharon Uy for the help with editing the paper. The authors thank Irina Zhelavskaya and Frederic Effenberger for useful discussions. The authors thank anonymous reviewers for the insightful comments.

References

Agapitov, O. V., Artemyev, A. V., Mourenas, D., Mozer, F. S., & Krasnoselskikh, V. (2015). Empirical model of lower band chorus wave distribution in the outer radiation belt. *Journal of Geophysical Research: Space Physics*, *120*, 10,425–10,442. https://doi.org/10.1002/2015JA021829

Agapitov, O. V., Mourenas, D., Artemyev, A. V., Mozer, F. S., Hospodarsky, G., Bonnell, J., & Krasnoselskikh, V. (2018). Synthetic empirical chorus wave model from combined Van Allen Probes and Cluster statistics. *Journal of Geophysical Research: Space Physics*, *123*, 297–314. https://doi.org/10.1002/2017JA024843

Albert, J. M. (2005). Evaluation of quasi-linear diffusion coefficients for whistler mode waves in a plasma with arbitrary density ratio. *Journal of Geophysical Research*, *110*, A03218. https://doi.org/10.1029/2004JA010844

Angelopoulos, V., Baumjohann, W., Kennel, C. F., Coroniti, F. V., Kivelson, M. G., Pellat, R., et al. (1992). Bursty bulk flows in the inner central plasma sheet. *Journal of Geophysical Research*, *97*(A4), 4027–4039. https://doi.org/10.1029/91JA02701

Angelopoulos, V., Kennel, C. F., Coroniti, F. V., Pellat, R., Kivelson, M. G., Walker, R. J., et al. (1994). Statistical characteristics of bursty bulk flow events. *Journal of Geophysical Research*, *99*(A11), 21,257–21,280. https://doi.org/10.1029/94JA01263

Aseev, N. A., Shprits, Y. Y., Drozdov, A. Y., & Kellerman, A. C. (2016). Numerical applications of the advective-diffusive codes for the inner magnetosphere. *Space Weather*, *14*, 993–1010. https://doi.org/10.1002/2016SW001484

Axford, W. I. (1969). Magnetospheric convection. *Reviews of Geophysics*, *7*(1-2), 421–459. https://doi.org/10.1029/RG007i001p00421

Baker, D. N. (2000). The occurrence of operational anomalies in spacecraft and their relationship to space weather. *IEEE Transactions on Plasma Science*, *28*(6), 2007–2016. https://doi.org/10.1109/27.902228

Blake, J. B., Carranza, P. A., Claudepierre, S. G., Clemmons, J. H., Crain, W. R., Dotan, Y., et al. (2013). The magnetic electron ion spectrometer (MagEIS) instruments aboard the Radiation Belt Storm Probes (RBSP) spacecraft. *Space Science Reviews*, *179*(1-4), 383–421. https://doi.org/10.1007/s11214-013-9991-8

Boscher, D., Bourdarie, S., O'Brien, P., & Guild, T. (2012). IRBEM-LIB library,http://irbem.sourceforge.net

Brautigam, D. H., & Albert, J. M. (2000). Radial diffusion analysis of outer radiation belt electrons during the October 9, 1990, magnetic storm. *Journal of Geophysical Research*, *105*(A1), 291–309. https://doi.org/10.1029/1999JA900344

Califf, S., Li, X., Blum, L., Jaynes, A., Schiller, Q., Zhao, H., et al. (2014). THEMIS, measurements of quasi-static electric fields in the inner magnetosphere. *Journal of Geophysical Research: Space Physics*, *119*, 9939–9951. https://doi.org/10.1002/2014JA020360

Califf, S., Li, X., Zhao, H., Kellerman, A., Sarris, T. E., Jaynes, A., & Malaspina, D. M. (2017). The role of the convection electric field in filling the slot region between the inner and outer radiation belts. *Journal of Geophysical Research: Space Physics*, *122*, 2051–2068. https://doi.org/10.1002/2016JA023657

Carpenter, D. L., & Anderson, R. R. (1992). An ISEE/whistler model of equatorial electron density in the magnetosphere. *Journal of Geophysical Research*, *97*(A2), 1097–1108. https://doi.org/10.1029/91JA01548

Chen, M. W., Lemon, C. L., Orlova, K., Shprits, Y., Hecht, J., & Walterscheid, R. L. (2015). Comparison of simulated and observed trapped and precipitating electron fluxes during a magnetic storm. *Geophysical Research Letters*, *42*, 8302–8311. https://doi.org/10.1002/2015GL065737

Choi, H.-S., Lee, J., Cho, K.-S., Kwak, Y.-S., Cho, I.-H., Park, Y.-D., et al. (2011). Analysis of GEO spacecraft anomalies: Space weather relationships. *Space Weather*, *9*, 06001. https://doi.org/10.1029/2010SW000597

Cornwall, J. M. (1968). Diffusion processes influenced by conjugate-point wave phenomena. *Radio science*, *3*(7), 740–744. https://doi.org/10.1002/rds196837740

DeForest, S. E. (1972). Spacecraft charging at synchronous orbit. *Journal of Geophysical Research*, *77*(4), 651–659. https://doi.org/10.1029/JA077i004p00651

Denton, M. H., Henderson, M. G., Jordanova, V. K., Thomsen, M. F., Borovsky, J. E., Woodroffe, J., et al. (2016). An improved empirical model of electron and ion fluxes at geosynchronous orbit based on upstream solar wind conditions. *Space Weather*, *14*, 511–523. https://doi.org/10.1002/2016SW001409

Denton, M. H., Reeves, G. D., Larsen, B. A., Friedel, R. F. W., Thomsen, M. F., Fernandes, P. A., et al. (2017). On the origin of low-energy electrons in the inner magnetosphere: Fluxes and pitch-angle distributions. *Journal of Geophysical Research: Space Physics*, *122*, 1789–1802. https://doi.org/10.1002/2016JA023648

Denton, M. H., Thomsen, M. F., Jordanova, V. K., Henderson, M. G., Borovsky, J. E., Denton, J. S., et al. (2015). An empirical model of electron and ion fluxes derived from observations at geosynchronous orbit. *Space Weather*, *13*, 233–249. https://doi.org/10.1002/2015SW001168

Dubyagin, S., Sergeev, V., Apatenkov, S., Angelopoulos, V., Runov, A., Nakamura, R., et al. (2011). Can flow bursts penetrate into the inner magnetosphere? *Geophysical Research Letters*, *38*, L08102. https://doi.org/10.1029/2011GL047016

Fok, M.-C., Buzulukova, N. Y., Chen, S.-H., Glocer, A., Nagai, T., Valek, P., & Perez, J. (2014). The Comprehensive Inner Magnetosphere-Ionosphere Model. *Journal of Geophysical Research: Space Physics*, *119*, 7522–7540. https://doi.org/10.1002/2014JA020239

Fok, M.-C., Glocer, A., Zheng, Q., Horne, R. B., Meredith, N. P., Albert, J. M., & Nagai, T. (2011). Recent developments in the radiation belt environment model. *Journal of Atmospheric and Solar-Terrestrial Physics*, *73*(11-12), 1435–1443. https://doi.org/10.1016/j.jastp.2010.09.033

Fok, M.-C., Moore, T. E., & Delcourt, D. C. (1999). Modeling of inner plasma sheet and ring current during substorms. *Journal of Geophysical Research*, *104*(A7), 14,557–14,569. https://doi.org/10.1029/1999JA900014

Foster, J. C., & Burke, W. J. (2002). SAPS: A new categorization for sub-auroral electric fields. *Eos, Transactions American Geophysical Union*, *83*(36), 393–394. https://doi.org/10.1029/2002EO000289

Foster, J. C., & Vo, H. B. (2002). Average characteristics and activity dependence of the subauroral polarization stream. *Journal of Geophysical Research*, *107*(A12), 1475. https://doi.org/10.1029/2002JA009409

Frank, L. A. (1967). Several observations of low-energy protons and electrons in the Earth's magnetosphere with OGO 3. *Journal of Geophysical Research*, *72*(7), 1905–1916. https://doi.org/10.1029/JZ072i007p01905

Friedel, R. H. W., Korth, H., Henderson, M. G., Thomsen, M. F., & Scudder, J. D. (2001). Plasma sheet access to the inner magnetosphere. *Journal of Geophysical Research*, *106*(A4), 5845–5858. https://doi.org/10.1029/2000JA003011

Funsten, H. O., Skoug, R. M., Guthrie, A. A., MacDonald, E. A., Baldonado, J. R., Harper, R. W., et al. (2013). Helium, Oxygen, Proton, and Electron (HOPE) mass spectrometer for the radiation belt storm probes mission. *Space Science Reviews*, *179*(1-4), 423–484. https://doi.org/10.1007/s11214-013-9968-7

Gabrielse, C., Angelopoulos, V., Runov, A., & Turner, D. L. (2012). The effects of transient, localized electric fields on equatorial electron acceleration and transport toward the inner magnetosphere. *Journal of Geophysical Research*, *117*, A10213. https://doi.org/10.1029/2012JA017873

Ganushkina, N. Y., Amariutei, O. A., Shprits, Y. Y., & Liemohn, M. W. (2013). Transport of the plasma sheet electrons to the geostationary distances. *Journal of Geophysical Research: Space Physics*, *118*, 82–98. https://doi.org/10.1029/2012JA017923

Ganushkina, N. Y., Amariutei, O. A., Welling, D., & Heynderickx, D. (2015). Nowcast model for low-energy electrons in the inner magnetosphere. *Space Weather*, *13*, 16–34. https://doi.org/10.1002/2014SW001098

Ganushkina, N., Jaynes, A., & Liemohn, M. (2017). Space weather effects produced by the ring current particles. *Space Science Reviews*, *212*(3-4), 1315–1344. https://doi.org/10.1007/s11214-017-0412-2

Ganushkina, N. Y., Liemohn, M. W., Amariutei, O. A., & Pitchford, D. (2014). Low-energy electrons (5–50 keV) in the inner magnetosphere. *Journal of Geophysical Research: Space Physics*, *119*, 246–259. https://doi.org/10.1002/2013JA019304

Goldstein, J., Burch, J. L., & Sandel, B. R. (2005). Magnetospheric model of subauroral polarization stream. *Journal of Geophysical Research*, *110*, A09222. https://doi.org/10.1029/2005JA011135

Gu, X., Shprits, Y. Y., & Ni, B. (2012). Parameterized lifetime of radiation belt electrons interacting with lower-band and upper-band oblique chorus waves. *Geophysical Research Letters*, *39*, L15102. https://doi.org/10.1029/2012GL052519

Horne, R. B., & Thorne, R. M. (1998). Potential waves for relativistic electron scattering and stochastic acceleration during magnetic storms. *Geophysical Research Letters*, *25*(15), 3011–3014. https://doi.org/10.1029/98GL01002

Horne, R. B., & Thorne, R. M. (2003). Relativistic electron acceleration and precipitation during resonant interactions with whistler-mode chorus. *Geophysical research letters*, *30*(10), 1527. https://doi.org/10.1029/2003GL016973

Horne, R. B., Thorne, R. M., Shprits, Y. Y., Meredith, N. P., Glauert, S. A., Smith, A. J., et al. (2005). Wave acceleration of electrons in the Van Allen radiation belts. *Nature*, *437*(7056), 227. https://doi.org/10.1038/nature03939

Hwang, J.-A., Lee, D.-Y., Lyons, L. R., Smith, A. J., Zou, S., Min, K. W., et al. (2007). Statistical significance of association between whistler-mode chorus enhancements and enhanced convection periods during high-speed streams. *Journal of Geophysical Research*, *112*, A09213. https://doi.org/10.1029/2007JA012388

Ilie, R., Liemohn, M. W., Toth, G., & Skoug, R. M. (2012). Kinetic model of the inner magnetosphere with arbitrary magnetic field. *Journal of Geophysical Research*, *117*, A04208. https://doi.org/10.1029/2011JA017189

Jordanova, V. K., Kistler, L. M., Kozyra, J. U., Khazanov, G. V., & Nagy, A. F. (1996). Collisional losses of ring current ions. *Journal of Geophysical Research*, *101*(A1), 111–126. https://doi.org/10.1029/95JA02000

Jordanova, V. K., & Miyoshi, Y. (2005). Relativistic model of ring current and radiation belt ions and electrons: Initial results. *Geophysical research letters*, *32*, L14104. https://doi.org/10.1029/2005GL023020

Jordanova, V. K., Tu, W., Chen, Y., Morley, S. K., Panaitescu, A.-D., Reeves, G. D., & Kletzing, C. A. (2016). RAM-SCB simulations of electron transport and plasma wave scattering during the October 2012 double-dip storm. *Journal of Geophysical Research: Space Physics*, *121*, 8712–8727. https://doi.org/10.1002/2016JA022470

Kletzing, C. A., Kurth, W. S., Acuna, M., MacDowall, R. J., Torbert, R. B., Averkamp, T., et al. (2013). The Electric and Magnetic Field Instrument Suite and Integrated Science (EMFISIS) on RBSP. *Space Science Reviews*, *179*(1-4), 127–181. https://doi.org/10.1007/s11214-013-9993-6

Korth, H., Thomsen, M. F., Borovsky, J. E., & McComas, D. J. (1999). Plasma sheet access to geosynchronous orbit. *Journal of Geophysical Research*, *104*(A11), 25,047–25,061. https://doi.org/10.1029/1999JA900292

Lejosne, S., Kunduri, B. S. R., Mozer, F. S., & Turner, D. L. (2018). Energetic electron injections deep into the inner magnetosphere: A result of the subauroral polarization stream (SAPS) potential drop. *Geophysical Research Letters*, *45*, 3811–3819. https://doi.org/10.1029/2018GL077969

Lemon, C., Wolf, R. A., Hill, T. W., Sazykin, S., Spiro, R. W., Toffoletto, F. R., et al. (2004). Magnetic storm ring current injection modeled with the Rice Convection Model and a self-consistent magnetic field. *Geophysical research letters*, *31*, L21801. https://doi.org/10.1029/2004GL020914

Li, W., Shprits, Y. Y., & Thorne, R. M. (2007). Dynamic evolution of energetic outer zone electrons due to wave-particle interactions during storms. *Journal of Geophysical Research*, *112*, A10220. https://doi.org/10.1029/2007JA012368

Liemohn, M. W., Kozyra, J. U., Clauer, C. R., & Ridley, A. J. (2001). Computational analysis of the near-Earth magnetospheric current system during two-phase decay storms. *Journal of Geophysical Research*, *106*(A12), 29,531–29,542. https://doi.org/10.1029/2001JA000045

Liu, J., Angelopoulos, V., Zhang, X.-J., Turner, D. L., Gabrielse, C., Runov, A., et al. (2016). Dipolarizing flux bundles in the cis-geosynchronous magnetosphere: Relationship between electric fields and energetic particle injections. *Journal of Geophysical Research: Space Physics*, *121*, 1362–1376. https://doi.org/10.1002/2015JA021691

Liu, S., Chen, M. W., Roeder, J. L., Lyons, L. R., & Schulz, M. (2005). Relative contribution of electrons to the stormtime total ring current energy content. *Geophysical research letters*, *32*, L03110. https://doi.org/10.1029/2004GL021672

Lyons, L. R., Gallardo-Lacourt, B., Zou, S., Weygand, J. M., Nishimura, Y., Li, W., et al. (2016). The 17 March 2013 storm: Synergy of observations related to electric field modes and their ionospheric and magnetospheric Effects. *Journal of Geophysical Research: Space Physics*, *121*, 10,880–10,897. https://doi.org/10.1002/2016JA023237

Lyons, L. R., & Schulz, M. (1989). Access of energetic particles to storm time ring current through enhanced radial diffusion. *Journal of Geophysical Research*, *94*(A5), 5491–5496. https://doi.org/10.1029/JA094iA05p05491

Lyons, L. R., & Williams, D. J. (1980). A source for the geomagnetic storm main phase ring current. *Journal of Geophysical Research*, *85*(A2), 523–530. https://doi.org/10.1029/JA085iA02p00523

Lyons, L. R., & Williams, D. J. (1984). *Quantitative aspects of magnetospheric physics, 231 pp. D*. Dordrecht-Boston-Lancaster: Reidel Publishing Company.

Maynard, N. C., & Chen, A. J. (1975). Isolated cold plasma regions: Observations and their relation to possible production mechanisms. *Journal of Geophysical Research*, *80*(7), 1009–1013. https://doi.org/10.1029/JA080i007p01009

Ohtani, S., Singer, H. J., & Mukai, T. (2006). Effects of the fast plasma sheet flow on the geosynchronous magnetic configuration: Geotail and GOES coordinated study. *Journal of Geophysical Research*, *111*, A01204. https://doi.org/10.1029/2005JA011383

Olson, W. P., & Pfitzer, K. A. (1977). Magnetospheric magnetic field modeling ann. sci. rep, Contract F44620-75-C-0033, Air Force Off. of Sci. Res. McDonnell Douglas Astronautics Co. Huntington Beach Calif.

Orlova, K., Shprits, Y., & Spasojevic, M. (2016). New global loss model of energetic and relativistic electrons based on Van Allen Probes measurements. *Journal of Geophysical Research: Space Physics*, *121*, 1308–1314. https://doi.org/10.1002/2015JA021878

Ozeke, L. G., Mann, I. R., Murphy, K. R., Jonathan Rae, I., & Milling, D. K. (2014). Analytic expressions for ULF wave radiation belt radial diffusion coefficients. *Journal of Geophysical Research: Space Physics*, *119*, 1587–1605. https://doi.org/10.1002/2013JA019204

Reeves, G. D., Friedel, R. H. W., Larsen, B. A., Skoug, R. M., Funsten, H. O., Claudepierre, S. G., et al. (2016). Energy-dependent dynamics of keV to MeV electrons in the inner zone, outer zone, and slot regions. *Journal of Geophysical Research: Space Physics*, *121*, 397–412. https://doi.org/10.1002/2015JA021569

Reeves, G. D., Spence, H. E., Henderson, M. G., Morley, S. K., Friedel, R. H. W., Funsten, H. O., et al. (2013). Electron acceleration in the heart of the Van Allen radiation belts. *Science*, *341*(6149), 991–994. https://doi.org/10.1126/science.1237743

Rowland, D. E., & Wygant, J. R. (1998). Dependence of the large-scale, inner magnetospheric electric field on geomagnetic activity. *Journal of Geophysical Research*, *103*(A7), 14,959–14,964. https://doi.org/10.1029/97JA03524

Runov, A., Angelopoulos, V., Sitnov, M. I., Sergeev, V. A., Bonnell, J., McFadden, J. P., et al. (2009). THEMIS observations of an earthward-propagating dipolarization front. *Geophysical Research Letters*, *36*, L14106. https://doi.org/10.1029/2009GL038980

Runov, A., Angelopoulos, V., Zhou, X.-Z., Zhang, X.-J., Li, S., Plaschke, F., & Bonnell, J. (2011). A THEMIS multicase study of dipolarization fronts in the magnetotail plasma sheet. *Journal of Geophysical Research*, *116*, A05216. https://doi.org/10.1029/2010JA016316

Sergeev, V. A., Chernyaev, I. A., Dubyagin, S. V., Miyashita, Y., Angelopoulos, V., Boakes, P. D., et al. (2012). Energetic particle injections to geostationary orbit: Relationship to flow bursts and magnetospheric state. *Journal of Geophysical Research*, *117*, A10207. https://doi.org/10.1029/2012JA017773

Shprits, Y. Y., Kellerman, A. C., Drozdov, A. Y., Spence, H. E., Reeves, G. D., & Baker, D. N. (2015). Combined convective and diffusive simulations: VERB-4D comparison with 17 March 2013 Van Allen Probes observations. *Geophysical Research Letters*, *42*, 9600–9608. https://doi.org/10.1002/2015GL065230

Shprits, Y. Y., Subbotin, D. A., Meredith, N. P., & Elkington, S. R. (2008). Review of modeling of losses and sources of relativistic electrons in the outer radiation belt II: Local acceleration and loss. *Journal of Atmospheric and Solar-Terrestrial Physics*, *70*(14), 1694–1713. https://doi.org/10.1016/j.jastp.2008.06.014

Southwood, D. J., & Wolf, R. A. (1978). An assessment of the role of precipitation in magnetospheric convection. *Journal of Geophysical Research*, *83*(A11), 5227–5232. https://doi.org/10.1029/JA083iA11p05227

Spasojevic, M., & Shprits, Y. Y. (2013). Chorus functional dependencies derived from CRRES data. *Geophysical Research Letters*, *40*, 3793–3797. https://doi.org/10.1002/grl.50755

Stern, D. P. (1975). The motion of a proton in the equatorial magnetosphere. *Journal of Geophysical Research*, *80*(4), 595–599. https://doi.org/10.1029/JA080i004p00595

Su, Y.-J., Selesnick, R. S., & Blake, J. B. (2016). Formation of the inner electron radiation belt by enhanced large-scale electric fields. *Journal of Geophysical Research: Space Physics*, *121*, 8508–8522. https://doi.org/10.1002/2016JA022881

Subbotin, D. A., & Shprits, Y. Y. (2012). Three-dimensional radiation belt simulations in terms of adiabatic invariants using a single numerical grid. *Journal of Geophysical Research*, *117*, A05205. https://doi.org/10.1029/2011JA017467

Summers, D., Thorne, R. M., & Xiao, F. (1998). Relativistic theory of wave-particle resonant diffusion with application to electron acceleration in the magnetosphere. *Journal of Geophysical Research*, *103*(A9), 20,487–20,500. https://doi.org/10.1029/98JA01740

Thébault, E., Finlay, C. C., Beggan, C. D., Alken, P., Aubert, J., Barrois, O., et al. (2015). International geomagnetic reference field: The 12th generation. *Earth, Planets and Space*, *67*(1), 79. https://doi.org/10.1186/s40623-015-0228-9

Thomsen, M. F., Henderson, M. G., & Jordanova, V. K. (2013). Statistical properties of the surface-charging environment at geosynchronous orbit. *Space Weather*, *11*, 237–244. https://doi.org/10.1002/swe.20049

Thorne, R. M. (2010). Radiation belt dynamics: The importance of wave-particle interactions. *Geophysical Research Letters*, *37*, L22107. https://doi.org/10.1029/2010GL044990

Toffoletto, F., Sazykin, S., Spiro, R., & Wolf, R. (2003). Inner magnetospheric modeling with the Rice Convection Model. *Space Science Reviews*, *107*(1-2), 175–196. https://doi.org/10.1023/A:1025532008047

Tsyganenko, N. A. (1989). A magnetospheric magnetic field model with a warped tail current sheet. *Planetary and Space Science*, *37*(1), 5–20. https://doi.org/10.1016/0032-0633(89)90066-4

Tsyganenko, N. A. (1995). Modeling the Earth's magnetospheric magnetic field confined within a realistic magnetopause. *Journal of Geophysical Research*, *100*(A4), 5599–5612. https://doi.org/10.1029/94JA03193

Tsyganenko, N. A. (2002). A model of the near magnetosphere with a dawn-dusk asymmetry 1. Mathematical structure. *Journal of Geophysical Research*, *107*(A8), SMP–12. https://doi.org/10.1029/2001JA000219

Tsyganenko, N. A., & Sitnov, M. I. (2005). Modeling the dynamics of the inner magnetosphere during strong geomagnetic storms. *Journal of Geophysical Research*, *110*, A03208. https://doi.org/10.1029/2004JA010798

Tsyganenko, N. A., & Sitnov, M. I. (2007). Magnetospheric configurations from a high-resolution data-based magnetic field model. *Journal of Geophysical Research*, *112*, A06225. https://doi.org/10.1029/2007JA012260

Turner, D. L., Claudepierre, S. G., Fennell, J. F., O'Brien, T. P., Blake, J. B., Lemon, C., et al. (2015). Energetic electron injections deep into the inner magnetosphere associated with substorm activity. *Geophysical Research Letters*, *42*, 2079–2087. https://doi.org/10.1002/2015GL063225

Volland, H. (1973). A semiempirical model of large-scale magnetospheric electric fields. *Journal of Geophysical Research*, *78*(1), 171–180. https://doi.org/10.1029/JA078i001p00171

Weimer, D. R. (2005). Improved ionospheric electrodynamic models and application to calculating Joule heating rates. *Journal of Geophysical Research*, *110*, A05306. https://doi.org/10.1029/2004JA010884

Wygant, J. R., Bonnell, J. W., Goetz, K., Ergun, R. E., Mozer, F. S., Bale, S. D., et al. (2013). The electric field and waves instruments on the Radiation Belt Storm Probes mission. In *The Van Allen Probes Mission* (pp. 183–220). Boston, MA: Springer. https://doi.org/10.1007/s11214-013-0013-7

Yu, Y., Jordanova, V. K., Ridley, A. J., Toth, G., & Heelis, R. (2017). Effects of electric field methods on modeling the midlatitude ionospheric electrodynamics and inner magnetosphere dynamics. *Journal of Geophysical Research: Space Physics*, *122*, 5321–5338. https://doi.org/10.1002/2016JA023850

Zhao, H., Li, X., Baker, D. N., Claudepierre, S. G., Fennell, J. F., Blake, J. B., et al. (2016). Ring current electron dynamics during geomagnetic storms based on the Van Allen Probes measurements. *Journal of Geophysical Research: Space Physics*, *121*, 3333–3346. https://doi.org/10.1002/2016JA022358

Zhelavskaya, I. S., Shprits, Y. Y., & Spasojević, M. (2017). Empirical modeling of the plasmasphere dynamics using neural networks. *Journal of Geophysical Research: Space Physics*, *122*, 11,227–11,244. https://doi.org/10.1002/2017JA024406